Advanced Assessment of Ductile Tearing in Nuclear Reactor Pressure Vessel Steel Using X-ray Tomography

Michael Daly[1*], Fabien Leonard[1], John K Sharples[2], Andrew H Sherry[1]

[1] Dalton Nuclear Institute, The University of Manchester, Pariser Building - G Floor, Sackville Street, Manchester, M13 9PL, UK
[2] AMEC Technical Services, Walton House, Birchwood Park, Warrington, Cheshire, WA3 6AT, UK
* Corresponding author: michael.daly@postgrad.manchester.ac.uk

Abstract Reactor pressure vessels (RPV) are manufactured from medium strength low allow ferritic steel specifically selected of its high toughness and weldability. The ability of the RPV to withstand crack propagation is crucial to maintaining the operational safety of the reactor plant. Current generations of RPV steels operate at sufficiently high temperatures to ensure that the material remains ductile during its service life. Furthermore, new materials are engineered to exhibit greater ductility and fracture toughness throughout their operating life. Therefore understanding and being able to predict the ductile fracture behaviour is critical for assuring the safety of RPV steels during operating conditions.

This paper presents the results of an experimental programme aimed at using 3D X-ray tomography to quantify the volume fraction of ductile voids in tested pre-cracked specimens manufactured from A508 Class 3 RPV steel.

The results indicate a high concentration of voids very close to the fracture surface and voids extending 3.6mm below the crack. The data and experimental methodology could be used to calibrate predictive mechanistically based models such as the Gurson-Tvergaard-Needlman (GTN).

Keywords Ductile, Tearing, Steel, X-ray, Tomography

1. Introduction

The mechanism of ductile fracture is characterised by the nucleation, growth and coalescence of voids at initiating particles. These particles are categorised as inclusions and second phase particles, and in ferritic steel are most often manganese sulphide (MnS) inclusions and metallic carbide particles (M_nC). The voids form at these particles within the volume of high plastic strain and triaxial stresses ahead of a crack-tip or stress concentrator.

Two nucleating processes have been observed [1]: voids formation by either decohesion of the interface between the matrix and the inclusion/particle, or by cracking of the inclusion/particle itself. Voids then grow under the influence of increasing plastic strain and high hydrostatic stress within the material. A crack will propagate once neighbouring voids coalesce and/or reach a critical size producing a macroscopic flaw. The coalescence of the voids can be considered as the final stage in the crack growth mechanism.

The larger particles nucleate voids at lower stresses and strains [2] . Smaller particles will start contributing to void nucleation when the material is subjected to greater plastic deformation. The nucleation of these smaller voids at proximity to smaller particles, often between larger voids or

microcracks where intense shear bands are present, may result in a void sheeting effect further contributing to void coalescence [3, 4].

The metallurgical characteristics of the microstructure, including the size and distribution of the initiating particles which can often concentrate close to or on the grain boundaries will contribute to the nucleation and coalescence process. The distribution of these particles may also be uneven within the material with banding regions of greater concentration of particles or varying grain sizes [5].

There exists a range of mechanistically based models that have been developed to describe the ductile fracture process. One of these is the Gurson-Tvergaard-Needleman (GTN) model [6] which characterises failure by defining a material yield function which depends greatly on the stress states and on material specific characteristics. These characteristics need to be calibrated to enable a simulation of ductile crack growth.

1.1 The Gurson Tvergaard Needleman

The GTN model assumes the material is homogeneous and behaves as a continuum with an idealised void volume fraction distribution. Crucially, the model takes into consideration both the strain softening effects of void nucleation, growth and coalescence as well as the competing effect of the matrix hardening behaviour to define a material yielding function Φ, defined as (Eq.1):

$$\Phi\left(\sigma_e,\sigma_m,\bar{\sigma},f^*\right)=\left(\frac{\sigma_e}{\bar{\sigma}}\right)^2+2q_1f^*\cosh\left(\frac{3q_2\sigma_m}{2\bar{\sigma}}\right)-\left(1+q_3f^{*2}\right)=0 \quad (1)$$

Where:
σ_e = macroscopic Von Mises Stress
σ_m = macroscopic mean stress
$\bar{\sigma}$ = flow stress for the matrix material
f^* = current void fraction

The values for q_1, q_2 and q_3 were introduced by Tvergaard and Needleman to better simulate the experimental observations. These are often taken as $q_1 = 1.5$, $q_2 = 1.0$ and $q_3 = q_1^2$. The rate of void growth is related to the plastic part of the strain rate tensor $\dot{\varepsilon}^p_{kk}$ and the void nucleation rate is related to the equivalent plastic strain rate, $\dot{\varepsilon}^p_{eq}$ in (Eq. 2):

$$f^*=f_{growth}+f_{nucleation}=(1-f)\dot{\varepsilon}^p_{kk}+\Lambda\dot{\varepsilon}^p_{eq} \quad (2)$$

The first term expresses the growth rate of existing voids assuming the matrix material is incompressible and the second term defines the quantity of new voids that have nucleated as a result of the increasing plastic strain.

The scaling coefficient, Λ is characterised by (Eq. 3):

$$\Lambda = \frac{f_N}{s_N\sqrt{2\pi}} \exp\left[-\frac{1}{2}\left(\frac{\varepsilon_{eq}^{p} - \varepsilon_N}{S_N}\right)^2\right] \quad (3)$$

Where:
f_N= volume fraction of void nucleating particles
s_N = standard deviation
ε_N = mean value
ε_{eq}^{P} = equivalent plastic strain.

An additional feature of the GTN model, introduced by Tvergaard and Needleman, was to take into consideration the initial void fraction f_0, a critical void volume fraction for coalescence f_c, and a critical void fraction that corresponds to the failure of the matrix, f_F.

$$f^* = \begin{cases} f & \text{for } f \le f_c \\ f_c - \dfrac{f_u^* - f_c}{f_F - f_c}(f - f_c) & \text{for } f > f_c \end{cases} \quad (4)$$

Where:
f_c = critical void volume fraction (typically $f_c = 0.15$ for carbon steel)
f_F = actual void volume fraction at final fracture
f_u^* = modified void volume fraction (typically $f_u^* = 1/q_1$)

The distribution of the initiating particles as well as their void volume fraction are key microstructural features that are needed to accurately calibrate the GTN model. These material specific parameters are usually calibrated using metallographic observations of the non-fractured material and the material volume around fractured test specimens from carefully controlled experiments. The fracture tests can be performed using a range of specimens introducing different levels of constraint and stress states. The highly constrained pre-cracked compact test (CT) specimen is frequently used to measure fracture toughness and will be used and discussed throughout this paper.

Previous experiments have shown that void volume fractions (VVF) may vary by material but also by specimen types. Work by Kerry et al [7] on a high strength and low toughness aluminium alloy AL2024-T351 have shown that there is a difference in the distribution of the void volume fraction below the fracture surface for notched tensile specimens when compared with CT specimens. Using 3D X-ray tomography Taylor et al demonstrated that the CT specimens exhibited a higher concentration of voids close to the fracture surface when compared with that measured close to the fracture surface in notched tensile specimens. On the other hand, the voids extended further below the fracture surface in notched tensile specimens than was observed in CT specimens.

Further work has recently been performed by Daly et al [8] with respect to an A508 Class 3 RPV ferritic steel to quantify the void volume fraction using 2D optical micrographs. Similar

observations showed a higher concentration of voids for pre-cracked specimens than for notched tensile specimens. Additionally, a greater analysis of the area below the fracture surface has shown that the void volume fraction can extend to a few millimetres below the fracture surface with large clusters of voids extending up to 3.5mm below the fracture surface.

The aim of this paper is to extend the observations made in this previous work by using 3D X-ray tomography to further quantify the void volume fraction below the fracture surface in pre-cracked CT specimens of A508 Class 3 RPV ferritic steel. The methodology and observations will be discussed as well as its implications for the calibration and application of the GTN model.

2. Experimental

2.1 Material

The material used throughout this experiment was an A508 Class 3 ferritic steel. The specimens were extracted from the outer ring of an upright wedge-shaped block originating from a larger ring forging. All the specimens were extracted from the same location and in the same orientation. The chemical composition (wt%) of the ferritic steel was evaluated using spectographic analysis and the results are indicated in Table 1.

Table 1: Chemical composition in wt% of A508 Class 3 steel.

C	Si	Mn	P	S	Cr	Mo	Ni	Al	Co	Cu	Sn	Ti	V
0.18	0.23	1.3	<0.005	<0.005	0.25	0.55	0.81	0.02	0.01	0.04	0.005	<0.01	0.01

2.2 Mechanical testing

The tensile properties of the material were determined using standard round-bar test specimens oriented in the hoop direction. Three tensile specimens were tested on a Zwick 1464 at room temperature using a strain rate of 0.025% s^{-1} according to BS EN ISO 6892 procedure [9].

Ten fracture toughness tests were performed according to the ESIS P2-92 [10] standard using CT specimens with standard dimensions of thickness, B = 25mm, width, W = 50mm and a crack length to specimen width ratio, a/W = 0.53. Specimens were 20% side-grooved following fatigue pre-cracking. Tests were performed using both the unloading compliance and the multi specimen methods. Out of the ten tested CT specimens, two were left intact in order to preserve the crack tip for analysis.

2.3 Metallographic analysis

The cracked and parent material was imaged using optical and scanning electron microscopes. The parent material was imaged to characterise the general microstructure of the ferritic steel with a specific interest on grain size and inclusion/particle type and distribution. The cracked specimens were analysed to characterise the ductile fracture mechanism and distribution of voids below the

fracture surface.

For the parent material, metallographic sections were taken to view the material in the axial-radial plane. The fractured sections were machined through the tested specimen halves in the region where plain strain fracture was expected to take place. The metallographic sections were progressively ground and polished to a mirror finish of 0.25 μm using diamond paste and etched using colloidal silica and 2% Nital.

2.4 X-ray Tomography Analysis

The test samples for X-ray tomography imaging were machined below the fracture surface of three CT specimens using electrical discharge machining (EDM). The samples were approximately 0.5mm in diameter and 12mm in length and were extracted at regular intervals starting at the pre-cracked region but before the initiation of ductile tearing. The remaining specimens were extracted from below the ductile crack path and beyond the crack arrest point. The sections were extracted as close as possible to the region where plane strain was expected to take place with the greatest amount of ductile tearing damage. The surfaces of these small cylinders were lightly polished to remove any rust or scaling resulting from the EDM.

The top 4mm very close to the fracture surface of these specimens were scanned at the Henry Moseley X-ray Imaging Facility at The University of Manchester using the Nikon Metrology 225/320 kV Custom Bay system equipped with a 225 kV static multi-metal anode source and a PerkinElmer 2000 × 2000 pixels 16-bit amorphous silicon flat panel detector.

The scanning was performed with a molybdenum target using a voltage of 80 kV and a current of 130 μA. The data acquisition was carried out with an exposure time of 1000 ms with no filtration. The number of projections was set to 3,142 and the number of frames per projection was 1. The entire volume was reconstructed at full resolution with a voxel size of 2.0 μm along the x, y, and z directions.

The data processing was performed with Avizo® Fire 7.0 software. An edge preserving smoothing filter was applied to the raw data to reduce image noise in each data set. Standard data processing was used to determine the void size distribution whereas a methodology similar to [11] was employed to determine the void to fracture surface distance and evolution of void volume fraction.

2.5 Quantification of ductile tearing damage

Using the Avizo Fire data, the void volume fraction was estimated by measuring the voxel counts of metallic voxels against the count of porous voxels below the fracture surface. The VVF was calculated for each Regions Of Interest (ROI). A ROI of 100μm in height was utilised to divide the specimens into smaller cylinder regions which were comparable to the units used in Daly et al [8]. The VVF was calculated for the specimens originating below the pre-cracked surface as well as the region below the ductile tearing surface and beyond the crack arrest.

3. Results

The results from the three tensile tests at room temperature are summarised in Table 2. The average yield stress was 446 MPa and the ultimate tensile stress was 594 MPa.

The fracture toughness properties of the A508 Class 3 steel are illustrated as a J R-curve in Figure 1 which includes data from both the unloading compliance tests and monotonically loaded tests presented together. The data from both test types are in agreement and the initiation toughness, measured by the intersection of the blunting line including 0.2 mm tearing and the power-law curve fit to the data is ~ 475 kJ/m^2. The specimens for tomography analysis were extracted from test samples B, G and C as these specimens were subjected to the most ductile tearing.

Table 2: Tensile Test results

Specimen No.	1	2	3	Average
Modulus (GPa):	211	210	208	210
0.2 % Stress (MPa):	445	457	436	446
UTS (MPa):	595	602	586	594
Elongation (%)	29	27	27	28
Reduction of Area (%)	75	75	74	75

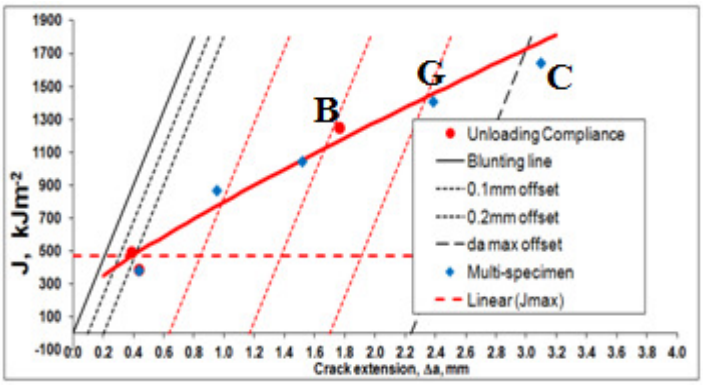

Figure 1: J R-curve for A508 Class 3 material tested in the hoop-radial direction at 23°C.

Figure 2 illustrates the general upper bainitic microstructure of the ferritic steel under the optical microscope and SEM respectively. The average grain size was estimated at 11µm. But the microstructure is interspersed with clusters of very small grains and regions where very large grains are present.

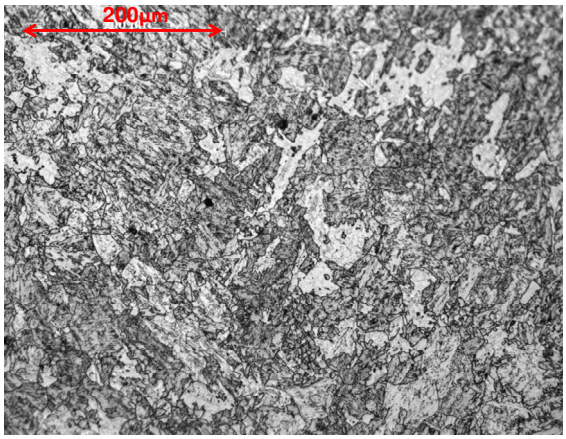

Figure 2: General microstructure of the bainitic steel under optical microscope.

Figure 3Figure 4 illustrate selected microstructural observations of voids in the material. Microvoids

were observed to initiate and grow by the decohesion of carbides from the matrix. Larger voids, in some cases, were shown to nucleate at large particles. These larger voids were observed to be present well below the fracture surface and ahead of the crack tip.

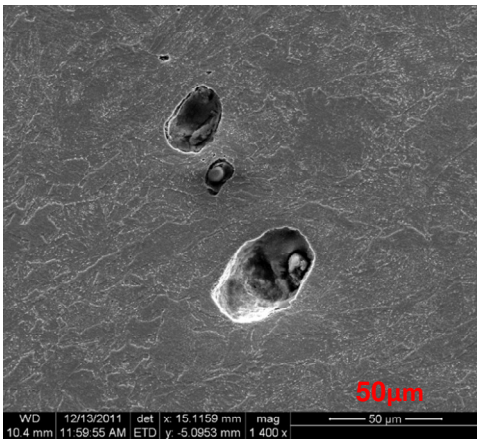

Figure 3: Large macroscopic voids with an inclusion

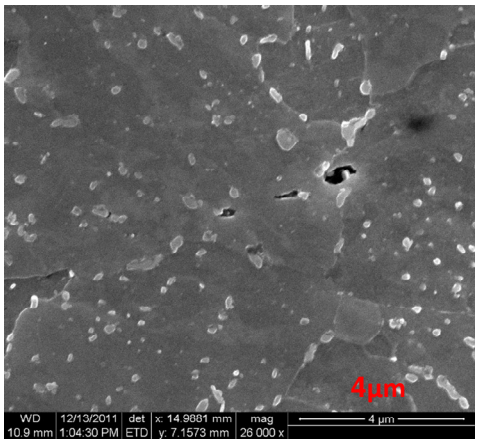

Figure 4: Microvoids nucleating at proximity of carbides

3.1 X-ray Tomography

The X-ray tomography images of Figure 5 shows the typical distribution of voids below the fracture surface for a specimen extracted from the fracture surface. Voids as small as 10µm in diameter could be resolved with a high degree of confidence. Figure 6 shows a render of the range of shapes and sizes of voids observed. Some voids have dumbbells morphologies possibly indicating coalescence. The ability to use the X-ray tomography technique enabled the imaging of voids in their entirety. Furthermore, this technique demonstrated the ability to visualise and quantify voids and in some cases, clusters of voids up to 3.6mm below the fracture surface.

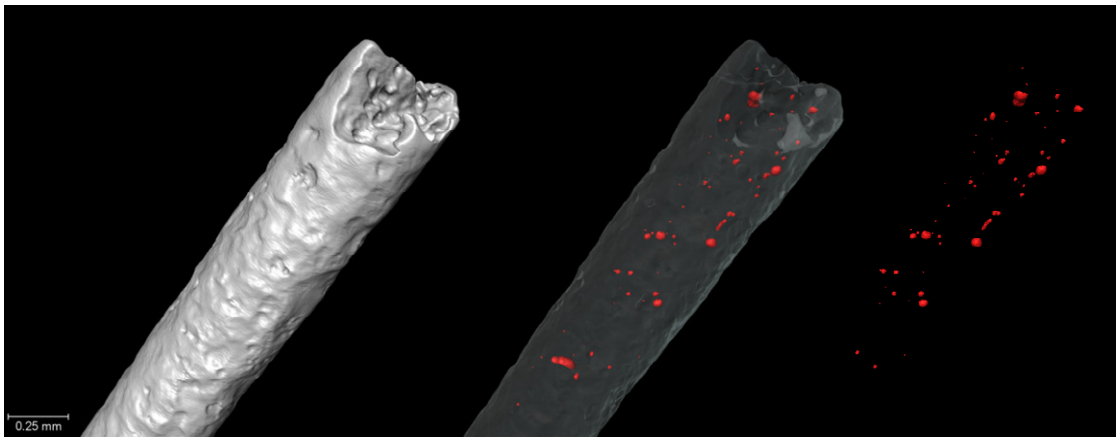

Figure 5: 3D tomographic image of the ferritic steel samples and the void distribution below the fracture surface.

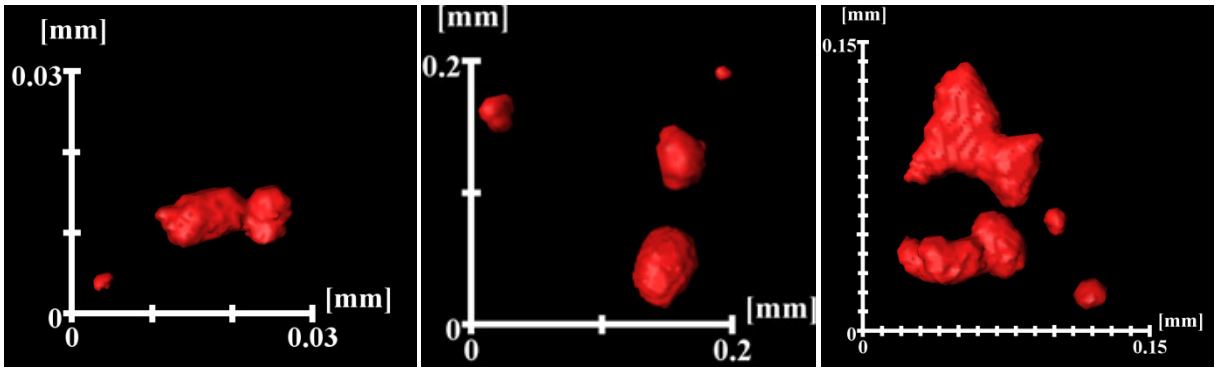

Figure 6: Magnified 3D tomographic images showing the range of sizes and shapes of voids quantified below the fracture surface.

3.2 Quantification results

The variation of the void volume fraction as a function of distance below the fracture surface in the CT specimens is illustrated in Figure **7**. The data were calculated by quantifying the average VVF for cylindrical cells of 100µm in height and starting from the fracture surface. The VVF for each specimen location (0mm, 0.5mm…) was averaged over all three specimens (B, C and G) to obtain an average VVF for the first 100µm below the fracture surface and every 100µm down to 3.6mm.

The presence of voids ahead of the final crack tip was also taking into consideration. Samples B and G had crack extensions of approximately 2mm, the extractions beyond the crack front were averaged separately and labeled as “beyond crack tip” on the plot.

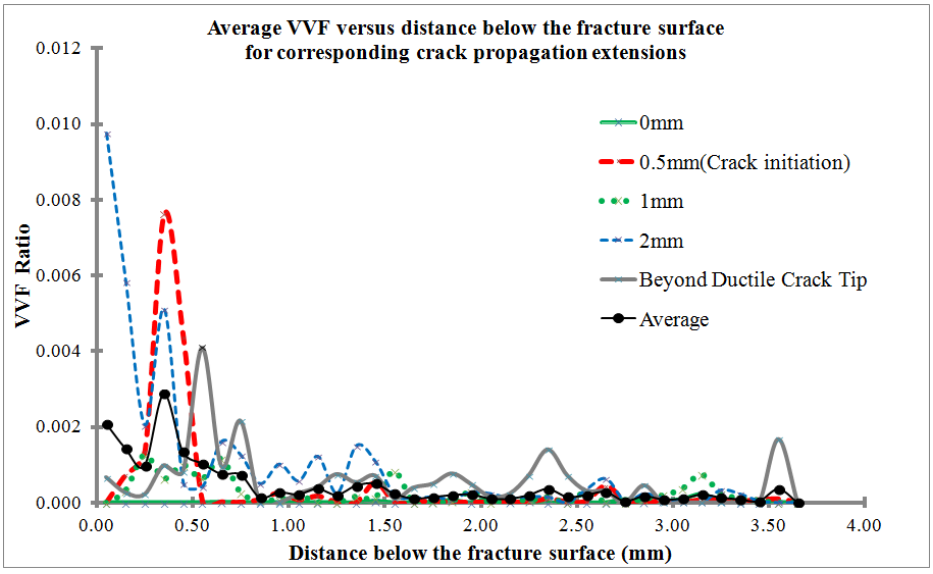

Figure 7: VVF as a function of distance below the fracture surface

The following observations can be made:

- The void volume fraction is highest close to the fracture surface and reduces to zero as a function of distance below the crack. A maximum VVF of 9.75×10^{-3} is measured

for the 2mm specimens. The VVF remains relatively high up to 800μm below the fracture surface.

- Secondary peaks are observed well below the fracture surface especially for the specimens extracted below extensive ductile tearing. The peaks are often representative of clusters of voids or very large voids at depths ranging from 1mm to 3.6mm.
- Pre-cracking of the fracture toughness specimens produces very little observable ductile tearing damage.
- At 2mm of ductile tearing, the ductile damage is immediately quantifiable very close to the fracture surface. For the other specimens, voids only become visible after 250μm below the fracture surface and peaks at a ratio of 7.60×10^{-3}.
- The data captured within the volume of material at proximity to the crack initiation and blunting (0.5mm) produce some of the highest VVF values with a maximum of 7.60×10^{-3} at 350μm below the crack surface.
- Voids have been imaged and quantified beyond the crack tips indicating ductile tearing damage ahead of the crack path.

4. Discussion

Taylor et al [7] quantified the void volume fraction below the fracture surface in failed CT specimens of AL2024-T351 aluminium alloy using optical and X-ray tomography. A critical void volume fraction f_f of approximately 1.0×10^{-2} was calculated for the aluminium alloy which compares favourably with the results obtained for the RPV ferritic steel of $f_f = 9.75\times10^{-3}$.

It is worth noting that the peaks within the void volume fraction data may disproportionately increase the average volume fraction well below the fracture surface for the three test specimens. But as the material should be considered as a continuum with an even distribution of initial voids and initiating particles, the average void volume fraction over a large number of tests should be representative of the material's bulk and fracture characteristics.

On the other hand, the ductile damage extends further beyond the crack surface in the ferritic steel than in the aluminium alloy. The aluminium alloy exhibits a sharp reduction in the VVF which reaches $f = 0$ at 300μm below the fracture surface. The ferritic steel exhibits ductile tearing damage up to 3.6 mm below the fracture surface identified by large voids and clusters of voids. The extent of the ductile damage was equally observed by previous work from Daly et al [8] using optical imaging analysis.

The substantial extent of the ductile damage was further observed in an equivalent HY100 ferritic steel. The work from Everett et al [2] identified voids below the fracture surface of fractured notched tensile specimens using a synchrotron source with equivalent resolutions. The distribution of voids deep below the fracture surface was attributed to microstructural banding and larger MnS inclusions. These larger MnS inclusions preferentially promoted the nucleation of voids at relatively low strains.

The effect of the plastic strain field produced from the propagating crack may provide sufficient strains at inclusions and particles to nucleate and grow relatively large voids deep below the fracture surface. A correlation of the experimental work with a finite element analysis is required to attain an estimate of the gradient of strains ahead and below the crack during propagation.

Finally, the tomographic images suffered from a blurring effect as a result of the X-ray beam hardening and X-ray spot being too large in comparison with the void sizes that were being imaged. Consequently, a substantial number of voids were only partially resolved and quantified since the pixel colours of these voids matched other metallic areas of the specimens and needed to be culled to obtain a reproducible and systematic quantifying tool. Further work will aim to use a synchrotron facility that will reduce such imaging artefacts and will ultimately increase the overall void volume fraction within the specimens.

5. Conclusions

This paper has described preliminary work undertaken to characterise the ductile fracture properties and fracture mechanism in A508 Class 3 steel using X-ray tomography analysis. The main conclusions from the work are as follows:

- The mechanical and fracture toughness properties have been quantified in the hoop direction. The average yield stress is 446 MPa and the initiation toughness defined by the 0.2 mm blunting line is ~ 475 kJ/m^2.
- The ductile fracture mechanism was identified to occur by the decohesion of the matrix from inclusions and second phase particles.
- The ductile damage was successfully imaged and quantified in 3D using X-ray laboratory sources to image voids of approximately 10µm in diameter and larger below the crack surface of compact test specimens.
- A relatively high VVF was quantified for specimens extracted at a 2mm crack extension but high concentrations of voids were also observed at 350µm and intermittently until 3600µm for specimens extracted along the length of the crack path. The results differ from experiments carried out with aluminium alloys where the VVF reached the background level at 300µm below the fracture surface.
- As a result of the limitations of the X-ray machine and software, a proportion of the voids were not quantified which has produced a VVF lower than is actually present in the material.
- The distribution of the voids deep below the fracture surface is attributed to microstructural banding and larger inclusions requiring lower strains.

6. Acknowledgements

The authors are grateful to AMEC in Risley for their support in the use of their material testing and

microscopy equipment. And, Fabien Leonard and Tristan Lowe from the University of Manchester Henry Moseley X-ray Imaging Facility for the use of the machines and their expertise.

7. References

[1] R. H. Van Stone, T. B. Cox, J. R. Low and J. A. Psioda, "Microstructural aspects of fracture by dimpled rupture," *International Metals Reviews ,* vol. 30, no. 4, pp. 157-179, 1985.

[2] R. K. Everett, K. E. Simmonds and A. B. Geltmacher, "Spatial distribution of voids in HY-100 Steel by X-ray Tomography," *Scripta Materialia,* vol. 44, pp. 165-169, 2001.

[3] T. Pardeon and J. W. Hutchinson, "An Extended Model for Void Growth and Coalescence," *Journal of the Mechanics and Physics of Solids,* vol. 48, pp. 2467-2512, 2000.

[4] V. Tvergaard, "Ductile Fracture by Cavity Nucleation Between Larger Voids," *Journal of the Mechanics and Physics of Solids,* vol. 30, pp. 265-286, 1982.

[5] C. I. A. Thomson, M. J. Worswick, A. K. Pilkey and D. J. Loyd, "Void Coalescence Within Periodic Clusters of Particles," *Journal of the Mechanics and Physics of Solids,* vol. 51, pp. 127-146, 2003.

[6] Z. L. Zhang, "A Complete Gurson Model," *Non Linear Fracture and Damage Mechanics,* pp. 223-248, 2001.

[7] K. L. Taylor and A. H. Sherry, "The characterization and interpretation of ductile fracture mechanisms in AL2024-T351 using X-ray and focused ion beam tomography," Vols. 60 (2012) 1300-1310, 2012.

[8] M. Daly, J. K. Sharples and A. H. Sherry, "Advanced Assessment of the Integrity of Ductile Components," in *ASME Pressure Vessels and Piping Division Conference*, Toronto, 2012.

[9] British Standards, ""Metallic materials. Tensile Testing. Method of test at ambient temperature" BS EN ISO 6892-1:2009".

[10] European Structural Integrity Society, "ESIS Standard No. P2-92: Procedure for determining the fracture behaviour of materials," ESIS, 1992.

[11] F. Leonard, J. Stein, A. Wilkinson and P. Withers, "3D Characterisation of Void Distribution in Resin Film Infused Composites," in *Conferene on Industrial Computed Tomography*, 2012.